Statistical effects in X-ray diffraction lattice strain measurements of ferritic steel using crystal plasticity

T.O. Erinosho[a], D.M. Collins[b,c], R.I. Todd[c], A.J. Wilkinson[c], F.P.E. Dunne[d]

[a]*Department of Mechanical Engineering, University of Bristol, Bristol, BS8 1TH, UK*
[b]*School of Metallurgy and Materials, University of Birmingham, Edgbaston, Birmingham, B15 2TT, UK*
[c]*Department of Materials, University of Oxford, Parks Road, Oxford, OX1 3PH, UK*
[d]*Department of Materials, Imperial College London, Exhibition Road, London SW7 2AZ, UK*

Abstract

The influence of statistics on calculated lattice strains has been studied by comparing crystal plasticity finite element (CPFE) calculations with strains measured experimentally. Experimentally, when Bragg's law is obeyed, a plane normal must lie within a narrow orientation range ($\sim 0.02^\circ$ for synchrotron diffraction), or Bragg tolerance. However, CPFE models consider only a small number of grains compared to experiments, necessitating a justification of the statistically representative volume. It also becomes necessary to assess the threshold of Bragg tolerance allowable for the determined statistically representative volume. In this study, an $8 \times 8 \times 8$ model was deemed as statistically representative such that only small benefits are obtained in terms of lattice strain calculations by adopting larger models such as $10 \times 10 \times 10$. Based on the selected model, an allowable Bragg tolerance of approximately 5° was calculated. Also highlighted was the coupling between lattice strain, texture, hardening and applied boundary condition which are discriminators that will affect the choice of model size and Bragg tolerance threshold.

Keywords: Lattice strain, statistics, crystal plasticity, X-ray diffraction, texture, hardening

1. Introduction

Methodologies that simulate diffraction patterns based upon deformation model results have been developed in recent years. Studies by Dawson and coworkers [1, 2] for example, have pioneered the computational approaches of predicting lattice spacing distributions. However, the limitations and constraints of the method have yet to be scrutinised. For example, self-consistent models (SCM) that have the capability of predicting deformation from a high number of grains comparable to that seen experimentally, crucially neglect grain constraint effects and cannot account for the strong intragrain variation (e.g in orientation) which develops. This is evident in Warwick *et al.* [3, 4] in which SCM were adopted to aid interpretation of neutron diffraction measurements of elastic strain partitioning in Ti-6Al-4V. Whilst excellent representations of average stress-strain behaviour were reproduced, the locally driven slip strengths extracted were less accurate.

The crystal plasticity finite element (CPFE) approach is advantageous over SCM for micromechanical studies in which intragranular detail is key since it captures localised effects. However, this approach is computationally

demanding and with current hardware constraints, simulating the number of grains typically measured in an X-ray diffraction experiment is impossible. In prior work [5, 6], a diffraction pattern simulation methodology was developed that used results obtained from a CPFE model. By relaxing the Bragg tolerance from the expected 0.02° typical of experimental diffraction to 5° in the simulation using crystal plasticity, good comparisons with experimental measurements were obtained. However, whilst increasing the Bragg angle reduces the statistical scatter in the calculated response, if the constraint is relaxed too far, information from grains that have different orientations and consequently different stress states will be sampled. This is problematic if grains in such conditions are absent in experimental measurements and leads to systematic errors. Therefore, this paper addresses the issue of statistics arising from increasing the Bragg tolerance in CPFE simulations, through a series of assessments needed to justify the choice of tolerance (e.g. 5° adopted in [5, 6]).

2. Experimental

An in-situ experiment on the I12 beamline at the Diamond Light Source was performed to obtain lattice strains during uniaxial and biaxial deformation. Specimens of a low-carbon single-phase ferritic steel, DX54, were deformed in-situ whilst collecting diffraction data. The specimens were deformed using a purpose built biaxial loading mechanism, controlled by a 10 kN Shimadzu AGS-X load frame. The specimens were of cruciform geometry with a locally reduced thickness (from 1 mm down to 400 μm) at the centre to provide a stress concentration in this region. Debye-Scherrer diffraction patterns were collected on a Thales Pixium area detector. As shown in Fig. 1a, the centre of the specimen was aligned normal to the incident X-ray beam, enabling diffraction data to be obtained from the locally thin region alone, in transmission. Displacements were applied to the cruciform arms, normal to the incident X-ray beam, as denoted by the arrows whilst diffraction data were collected. The sample orientation provides information from lattice planes approximately in the plane of the specimen. Calibrated with a CeO_2 standard [7], a beam energy of 90.36 keV and a sample to detector distance of 1125 mm provided lattice plane reflections up to $N = 10$ (where $N = h^2 + k^2 + l^2$ for lattice plane hkl). A beam size of 0.5×0.5 mm^2 was selected with diffraction spectra summed in a 4-point grid pattern with no overlap to illuminate a sufficiently large number of grains. The collected diffraction patterns were radially integrated into 36 sectors of equal 10° spacing using the FIT2D [8] software to provide intensity versus the diffraction angle, 2θ, data. The first sector, parallel to the direction 'X' in Fig. 1a corresponds to an azimuthal angle range between $\psi = -5°$ and $\psi = +5°$. The positions of the reflections in each sector were analysed using routines written in MATLAB, using a pseudo-Voigt function to fit each peak. Lattice spacings, d, were calculated from Bragg's law and lattice strains were obtained from $\epsilon_{hkl} = \frac{d-d_0}{d_0}$ where d_0 is the undeformed lattice spacing from a reference specimen. The initial reference lattice parameter, a_0 value was determined as 2.03647 Å and $d_0 = a_0/\sqrt{N}$. Further details of this experiment are available in ref [9].

To assist post-experiment analysis, the initial condition of the material was characterised using electron backscatter diffraction (EBSD) to provide spatially resolved map of grain orientations. A specimen of undeformed DX54 was

examined using a JEOL 6500F scanning electron microscope equipped with a TSL/EDAX OIM v6 EBSD system. The microscope was operated with a 14 nA beam current and an accelerating voltage of 20 keV. A region with dimensions 900 μm × 900 μm with a step size of 0.5 μm was assessed.

3. Crystal Plasticity Framework

The crystal plasticity framework adopted here is based on the kinematic decomposition of the deformation gradient, $\mathbf{F}$, into elastic, $\mathbf{F^e}$, and plastic, $\mathbf{F^p}$, tensors [10], where $\mathbf{F} = \mathbf{F^e F^p}$. and detailed in previous studies by Erinosho *et al.* [11, 12]. The slip rate for a given slip system is given by [13]

$$\dot{\gamma}^{\alpha} = \dot{\gamma}_0^{\alpha} \left| \frac{\tau^{\alpha}}{g^{\alpha}} \right|^{n} \operatorname{sgn}(\dot{\gamma}) \tag{1}$$

where the slip rate ($\dot{\gamma}^{\alpha}$) on slip system, α, is given by the reference strain rate, $\dot{\gamma}_0^{\alpha}$, resolved shear stress, τ^{α}, and slip system strength, g_{α}. Full details of this model may be found in [14, 15]. The evolution of slip system strength g_{α} is given by [16]

$$\dot{g}_{\alpha} = h_0 \left(1 + \frac{h_0 \Gamma}{\tau_0 m} \right)^{m-1} \dot{\gamma}_{\alpha} \tag{2}$$

in which a hardening modulus h_0, and parameter, m for the ferritic steel being investigated are adopted from Erinosho *et al.* [11]. The accumulated slip, Γ, depends on the two forms of hardening being investigated; self ($\Gamma = \gamma_{\alpha}$) and isotropic ($\Gamma = \gamma_{\text{sum}}$). These are further defined by [17]

$$\gamma_{\alpha} = \int_0^t \dot{\gamma}_{\alpha} \mathrm{d}t. \tag{3}$$

$$\gamma_{\text{sum}} = \sum_{\alpha=1}^{N_{\text{slip}}} \gamma_{\alpha}. \tag{4}$$

Under self-hardening, only active slip systems undergo hardening hence, $\dot{\gamma}_{\alpha}$ in Eq. 3 depends only on the slip on that particular slip system. Alternatively, isotropic hardening permits slip systems whether active or otherwise to undergo the same level of hardening. 24 BCC slip systems comprising 12 $\{110\}\langle 11\bar{1}\rangle$ and $\{112\}\langle 11\bar{1}\rangle$ families were considered.

Four oligocrystals comprising $5\times5\times5$, $6\times6\times6$, $8\times8\times8$ and $10\times10\times10$ grains as shown in Fig. 1b were studied. Each grain was a cube containing $6\times6\times6$ elements. Each grain is shown as a single colour. The boundary conditions set the positive surfaces to remain planar throughout the deformation and negative faces were constrained to move in their respective directions. Displacements were applied to the $+Y$-surface under uniaxial straining and to the $+X$ and $+Y$-surfaces under biaxial straining. Two textures were considered; a numerically generated random texture and an experimental texture typical of ferritic steel comprising many thousands of grains, obtained from electron backscatter diffraction, published elsewhere [9]. The {100} pole figures of the textured and random textures adopted in the models

are shown in Fig. 1b. The orientation selection and grain assignment between experiment to model was adopted by methods proposed elsewhere [18, 19, 20].

4. Simulation of diffraction data

Results from the CPFE model were used to calculate lattice strains for the high multiplicity {310} reflection using a previously developed method of simulating diffraction data [5]. The schematic in Fig. 1c shows the virtual geometry applied to a diffracting crystal. For every element in the model, lattice plane normals, $\mathbf{r}_{hkl}$, are calculated. This is defined by

$$\mathbf{r}_{hkl} = \Delta\mathbf{R}^{\mathbf{c}}\mathbf{R}_{\mathbf{0}}^{\mathbf{c}}\begin{bmatrix} h \\ k \\ l \end{bmatrix} \tag{5}$$

where $\mathbf{R}_{\mathbf{0}}^{\mathbf{c}}$ is a rotation matrix describing the undeformed crystal from the reference frame to the local crystallographic configuration and $\Delta\mathbf{R}^{\mathbf{c}}$ rotates the local crystal orientation into the deformed state. An example $\mathbf{r}_{hkl}$ is shown in Fig. 1c from a diffracting (310) plane, lying in an arbitrarily rotated cubic lattice. The forward projection, $\mathbf{s}_0$, onto a virtual detector screen is

$$\mathbf{s}_0 = \begin{bmatrix} r_{hkl_x} \\ r_{hkl_y} \\ 0 \end{bmatrix} \tag{6}$$

where r_{hkl_x} and r_{hkl_y} represent the x and y components of the rotated hkl plane normal. The angle, θ_0, between these two vectors, normalised, is $\theta_0 = \cos^{-1}(\hat{\mathbf{s}}_0 \cdot \hat{\mathbf{r}}_{\mathbf{hkl}})$. Diffraction is only satisfied if $\theta_0 = \theta_\mathrm{b}$ (from Bragg's law, $\theta_\mathrm{b} = \sin^{-1}(\lambda/2d_{hkl})$, where λ is the X-ray beam wavelength and d_{hkl} is the interplanar spacing). The angle θ_0 determines the angle of the diffracted beam from the direct beam, $2\theta_0$, as shown in Fig 1c. Experimentally, Bragg's law is obeyed within a finite angular range ($2\theta_\mathrm{b} \pm \delta\theta_\mathrm{b}$ where $\delta\theta_\mathrm{b}$ is hereon termed the Bragg tolerance) that is dependent on the X-ray source. If Bragg's law is satisfied, a diffraction spot appears on the detector at a position $\hat{\mathbf{s}}_0 L \tan 2\theta_0$ where L is the crystal to detector distance and the origin is defined as the centre of the virtual screen. Next, the azimuthal angle of the diffracted beam is calculated;

$$\psi = \tan^{-1}\left(\frac{r_{hkl_y}}{r_{hkl_x}}\right) \tag{7}$$

For polycrystalline samples, rings are observed as Bragg's law is satisfied for different azimuthal angles. Each diffraction spot recorded on the detector corresponds to a plane within a crystal (or element within the computational framework) and contains information on its crystallographic orientation as well as the orthorhombic (i.e. distorted cubic) lattice parameters. The latter were calculated from the elastic deformation tensor, $\mathbf{F}^{\mathbf{e}}$, using

$$\frac{a}{a_0} = |\mathbf{F^e}\hat{\mathbf{e}}_\mathbf{a}|, \quad \frac{b}{b_0} = |\mathbf{F^e}\hat{\mathbf{e}}_\mathbf{b}|, \quad \frac{c}{c_0} = |\mathbf{F^e}\hat{\mathbf{e}}_\mathbf{c}| \tag{8}$$

where a_0, b_0 & c_0 are the reference lattice parameters and $\hat{\mathbf{e}}_\mathbf{a}$, $\hat{\mathbf{e}}_\mathbf{b}$ & $\hat{\mathbf{e}}_\mathbf{c}$ are unit orthogonal vectors rotated into the deformed crystallographic configuration. Virtual diffraction patterns were radially integrated and lattice strains calculated using the same method applied to the experimental data.

5. Results & Discussion

The evolution of lattice strain for an $8 \times 8 \times 8$ grain model with an experimental texture subjected to two dissimilar strain-paths is presented in Fig. 2. The strain-paths considered are uniaxial shown in (a-c), and biaxial straining shown in (d-f). The evolution of the {310} lattice strain as a function of azimuthal angle, is shown, with the colours representing the lattice strain magnitude. Also shown is the measured experimental macroscopic deformation history Fig. 2aii & 2diii for each strain path, which was then replicated in the CPFE model. The results show the effect of changing the Bragg tolerance, $\delta\theta_\mathrm{b}$ and hardening law on the simulated lattice strains. For uniaxial deformation, in the experiment, the lattice strain becomes tensile close to $\psi = 90°$, parallel to the tensile axis, and compressive perpendicular due to Poisson contraction. For the biaxial case, the lattice strain distributes quite uniformly with respect to azimuthal angle, indicating all diffracting planes are experiencing the same response. The success in replicating this response via simulation is seen to be sensitive to $\delta\theta_\mathrm{b}$. Instead of using a typical experimental tolerance of 0.02°, the tolerance in the CPFE simulations is progressively increased from 0.5° to 10°. Increasing $\delta\theta_\mathrm{b}$ provides an increasingly smooth lattice spacing distribution compared to the noisy distribution when $\delta\theta_\mathrm{b} = 0.5°$. Increasing $\delta\theta_\mathrm{b}$ is seen to reduce the maximum simulated lattice strain, resulting from the range of stress states sampled from the simulated diffracting grains. Self-hardening expectedly produced a lower magnitude of lattice strain compared to isotropic hardening, irrespective of $\delta\theta_\mathrm{b}$. The maximum lattice strains predicted by isotropic hardening are far greater than those measured experimentally. This indicates the dislocation hardening rate predicted by isotropic hardening is much greater than is found experimentally. By visual inspection, self-hardening provides better agreement with the experimental data, for both uniaxial and biaxial deformation.

The effect of the modelled number of grains is shown in Fig. 3a, considering the smallest model comprising 125 grains ($5 \times 5 \times 5$) up to the largest 1000 grain ($10 \times 10 \times 10$) simulation. Fig. 3a shows the linear scaling of the number of diffracting grains (observed for all sectors between $\psi = 0°$ and $\psi = 180°$) as a function of $\delta\theta_\mathrm{b}$ and the model size (total number of simulated grains). To assess how the number of diffracting grains and hence model size affects the simulated lattice strains, a simple deformation case is considered. Using a set of crystal orientations with no preferred texture, samples were subjected to balanced biaxial straining to $\epsilon_X = \epsilon_Y = 5\%$. In this example, the macroscopic stress about the azimuthal plane (XY) is uniform with ψ. When measured experimentally via diffraction from a sample with a large number of grains, a constant lattice strain with ψ is observed i.e. [9]. For data binned into sectors, the average lattice strain per sector would be constant, however, if the number of diffracting grains within that sector reduces,

the effect of grains that have lattice strains that differ from the mean sector lattice strain becomes more pronounced. This behaviour is demonstrated in Fig. 3b for models of difference size with $\delta\theta_b = 5°$, showing the square difference between the mean lattice strain within a sector and the mean lattice strain for all sectors. This tests the statistics within the model alone (irrespective of the constitutive law). When the scatter within the model is equal to the difference between the experimental strains and the model, it is no longer possible to quantify any model improvements. It is seen that reducing the model size gives increasing lattice strain scatter with azimuthal angle, which poses the challenge to define what level of scatter is acceptable. If the purpose of the model is to capture lattice strain trends, then any model size of $8 \times 8 \times 8$ grains or greater is shown to give an approximate uniform square deviation with ψ. This would provide the correct conclusion that lattice strain is uniformly distributed about the azimuthal plane.

Next an error parameter, R is introduced to describe the fidelity between experimental, ϵ_e^j and simulated ϵ_s^j, lattice strains for a sector number, j, where $j = 1$ corresponds to $0° < \psi < 10°$; $R^j = (\epsilon_s^j - \epsilon_e^j)^2$. Here, the sample is again subjected to biaxial straining to $\epsilon_X = \epsilon_Y = 5\%$, however, the model adopts an experimental texture. The effect of the Bragg tolerance and model size is investigated by summing the values of R^j for all sectors, as shown in Fig. 3c. Here, an isotropic hardening model was used. The results show the greatest scatter (high ΣR) occur for when fewer grains are modelled or when $\delta\theta_b$ is small. The $8 \times 8 \times 8$ model size has the lowest ΣR when $\delta\theta_b > 1°$. The value of ΣR does not reduce further when $\delta\theta_b > 5°$. Increasing the Bragg tolerance beyond 5° should be avoided as no reduction in statistical noise is evident, while inclusion of different orientations and strain states may lead to systematic errors.

Simulated lattice strains may also be affected by texture. Fig. 3d uses the $8 \times 8 \times 8$ model from Fig 3a and an equivalent model with the experimental texture. Here, irrespective of $\delta\theta_b$, the texture used in this study gives $\sim 20\%$ fewer diffracting grains than a material with a random texture. This number is clearly texture dependent, but could be significant for (1) stronger initial textures or (2) textures developing at high strains.

With the $8 \times 8 \times 8$ model size justified, the choice of $\delta\theta_b$ and hardening model is finally decided in a comparison of uniaxial ($\epsilon_Y = 5\%$) and biaxial ($\epsilon_X = \epsilon_Y = 5\%$) straining. As shown in Fig. 4, the average square of deviation, R, gives a decrease in scatter with increasing $\delta\theta_b$, for both uniaxial and biaxial straining. However, for differing hardening forms, it is apparent that biaxial straining is more sensitive to $\delta\theta_b$ than uniaxial deformation. This is attributed to the fact that the rate of work hardening under biaxial is double that of uniaxial straining [5]. For this reason, the differences due to hardening are expected to be more pronounced under biaxial straining. This demonstrates that using the biaxial straining model as a discriminator for parameter selection was suitable. The prior conclusion of the most suitable hardening model from colour plots in Fig. 2 indicated that isotropic hardening overestimates the lattice strain magnitudes. This is supported by R values for uniaxial deformation reported in Fig. 4c (isotropic hardening) over Fig. 4d self hardening. However, isotropic hardening for biaxial deformation when $\delta\theta_b > 5°$ gives lower values of R compared to the equivalent self-hardening case. It appears that the increased hardening for biaxial deformation over uniaxial straining is simply better predicted using the isotropic hardening model. Clearly neither hardening model is perfect, however, their results are not sufficiently different to change the selection of $\delta\theta_b$.

The number of diffracting grains in both the experimental and simulated cases can be approximated to provide

further comparison between the two cases. In the experimental case, the volume probed by X-rays was $0.5 \times 0.5 \times 0.4\,\mathrm{mm}^3$. From an EBSD analysis of the initial material condition, shown as inverse pole figure in Fig. 5a, the mean grain size was ~12.5μm, giving approximately ~ 2.4×10^4 grains (N_g) in the probed volume. For simplification, the orientation of each crystal is assumed to be random. Analysis of the EBSD data shows that a small but non-negligible misorientation is present within each crystal, shown in Fig. 5b. This misorientation is plotted as a histogram in Fig. 5c; the fitted distribution shows the mean average crystal misorientation, φ, is 0.19°. The following calculation will demonstrate how misorientation heavily determines the number of diffracting planes measured experimentally.

The diffraction geometry is considered here in spherical space, as shown in Fig. 5 (d). A diffraction signal is measured only if scattered X-rays intersect the area A_b; an area determined by the width of the azimuthal sector ($\delta\psi$) and the Bragg tolerance, $\delta\theta_\mathrm{b}$.

$$A_\mathrm{b} = \int_{-\delta\psi/2}^{\delta\psi/2} \int_{2\theta_\mathrm{b}-\delta\theta_\mathrm{b}}^{2\theta_\mathrm{b}+\delta\theta_\mathrm{b}} \sin\theta \, \mathrm{d}\theta \, \mathrm{d}\psi \tag{9}$$

The geometry shows an incident beam directed towards a lattice plane (with normal $\mathbf{r}_{hkl}$) that scatters (shown as vector $\mathbf{D}$) at angle $2\theta_0$ to the incident beam direction. For the example (310) plane shown, its plane normal $\mathbf{r}^{(1)}_{hkl}$ represents the mean average orientation for the (310) lattice plane in that crystal. Its scattered vector $\mathbf{D}^{(1)}$ does not intersect A_b and therefore Bragg diffraction is not observed. However, where the crystal has misorientation, the (310) lattice plane will also be misorientated. Based on the EBSD analysis, the lattice plane exhibits an orientation range within this crystal. Hence, $\mathbf{r}_{hkl}$ has an orientation range that falls within a cone (as shown in Fig. 5d) with an opening angle 2φ at the vertex. Hence, the misorientation within this crystal is sufficient for a (310) plane with normal $\mathbf{r}^{(2)}_{hkl}$ to be scattered with vector $\mathbf{D}^{(2)}$ and now intersects A_b. This step is important as it determines how far away the mean orientation of a crystal can be for any part of the misorinentated crystal to obey the Bragg condition. If one is to use the mean crystal orientation to determine the number of diffracting planes, the area A_b condition can be modified to include misorientation. Accounting for crystal misorientation, a crystal will diffract if the mean crystal orientation yields scattered X-rays that intersect the area A^M_b, approximated as

$$A^\mathrm{M}_\mathrm{b} \approx \int_{-\frac{\delta\psi}{2}-\varphi}^{\frac{\delta\psi}{2}+\varphi} \int_{2\theta_\mathrm{b}-\delta\theta_\mathrm{b}-\varphi}^{2\theta_\mathrm{b}+\delta\theta_\mathrm{b}+\varphi} \sin\theta \, \mathrm{d}\theta \, \mathrm{d}\psi \tag{10}$$

Assuming the orientation of all crystals in the material is random, the distribution of plane normals $\mathbf{r}_{hkl}$ can also be considered random. The total number of diffracting grains, for a given hkl, N_D, is given by

$$N_\mathrm{D} = N_\mathrm{g} m \frac{A^\mathrm{M}_\mathrm{b}}{4\pi} \tag{11}$$

where m is the lattice plane multiplicity. Experimentally $\delta\theta_\mathrm{b} = 0.02°$, the azimuthal sector width $\delta\psi = 10°$ and the multiplicity of the {310} lattice planes is 24. These values correspond to ~40 grains diffracting from the {310} per azimuthal sector. During in-situ loading, 4 diffraction patterns were summed for each measurement point, giving ~160 grains in total per sector. This number is approximately an order of magnitude greater than the number of grains

simulated (as shown for all 18 sectors in Fig. 3a). For a single sector for simulated data where no initial misorientation is present ($\varphi = 0°$), N_D is 4 or 5 grains. This indicates that if a lattice plane of lower multiplicity was considered, i.e. {200}, only ~1 grain or for {110}, ~2 grains would be expected to diffract per sector when $\delta\theta_b = 5°$ and $8 \times 8 \times 8$ grains are simulated. As shown in Fig. 3d the presence of texture gives even fewer grains diffracting, making these lower multiplicity reflections unsuitable for use unless simulations with more grains are modelled.

6. Conclusion

This study serves to provide a pragmatic guide to the number of grains needed for a given Bragg threshold, where the right balance between the two must be identified for suitable comparisons to experimental data. A systematic study that compares the influence of parameters selected to simulate {310} lattice strains from CPFE models with experimental measurements has been undertaken. The analysis presented in this paper provided clear justifications on the choice of parameters when attempting to numerically calculate lattice strains in comparison with experiments. More specifically:

- The limitations of CPFE in modelling large grain sets required a sensitivity on the optimal grain set size. The results showed that the 8×8×8 model provided optimal results compared with the other oligocrystals considered (i.e. $5 \times 5 \times 5$, $6 \times 6 \times 6$ and $10 \times 10 \times 10$).

- In order to obtain less spurious lattice strain estimates from CPFE, the experimental Bragg tolerance ($\delta\theta_b = 0.02°$) can be relaxed. However, over-relaxing of the Bragg tolerance ($\delta\theta_b$) leads to averaging of lattice strains from grains of dissimilar orientation. This paper showed that for the $8 \times 8 \times 8$ model adopted, relaxing the $\delta\theta_b$ up to 5° provided optimal lattice strain calculations from CPFE in comparison with experiment.

- There is a coupling between hardening and nature of boundary conditions applied when comparing CPFE lattice strain calculations and experiment. The current study shows that biaxial straining is more sensitive to $\delta\theta_b$ than uniaxial deformation. This is attributed to the double rate of work hardening seen under biaxial straining compared with uniaxial. Therefore, biaxial loading should be adopted as a discriminator for parameter selection.

- The presence of texture was shown to influence the number of grains diffracting; ~20% fewer grains diffract in a texture polycrystal compared to a random texture. Therefore, the nature of texture should be considered as a discriminator for diffraction simulation parameter selection since an increased influence may be observed for (1) stronger initial textures or (2) textures developing at high strains.

- Diffraction plane multiplicity also influences the comparison between CPFE and experimentally measured lattice strain. The {310} family of planes was selected due to its higher multiplicity compared to other families such as {110} or {200}. Lower multiplicity reflections could be analysed, however, the total number of grains simulated would need to be increased to provide results that give the correct deformation response that is independent of diffraction statistics.

Acknowledgments

Funding has been provided by EPSRC (grant EP/I021043/1) with material and guidance from BMW-MINI gratefully acknowledged. With thanks also to the Diamond Light Source for the allocation of beamtime EE9333-1 on the I12 instrument. Data published in the manuscript will be made available via ora.ox.ac.uk.

References

[1] Obstalecki, M., Wong, S.L., Dawson, P.R., Miller, M.P.. Acta Mater 2014;75:259 – 272.

[2] Wong, S.L., Park, J.S., Miller, M.P., Dawson, P.R.. Comput Mater Sci 2013;77:456 – 466.

[3] Warwick, J.L.W., Coakley, J., Raghunathan, S.L., Talling, R.J., Dye, D.. Acta Mater 2012;60(10):4117 – 4127.

[4] Warwick, J.L.W., Jones, N.G., Rahman, K.M., Dye, D.. Acta Mater 2012;60(19):6720 – 6731.

[5] Erinosho, T.O., Collins, D.M., Wilkinson, A.J., Todd, R.I., Dunne, F.P.E.. Int J Plast 2016;83:1–18.

[6] Collins, D.M., Erinosho, T., Dunne, F.P.E., Todd, R.I., Connolley, T., Mostafavi, M., et al. Acta Mater 2017;124:290–304.

[7] Hart, M.L., Drakopoulos, M., Reinhard, C., Connolley, T.. J Appl Crystallogr 2013;46:1249–1260.

[8] FIT2D. http://www.esrf.eu/computing/scientific/FIT2D/; Accessed March 2014.

[9] Collins, D.M., Mostafavi, M., Todd, R.I., Connolley, T., Wilkinson, A.J.. Acta Mater 2015;90:46 – 58.

[10] Lee, E.H.. J Appl Mech 1969;36:1–6.

[11] Erinosho, T.O., Cocks, A.C.F., Dunne, F.P.E.. Int J Plast 2013;50:170 – 192.

[12] Erinosho, T.O., Cocks, A.C.F., Dunne, F.P.E.. Comput Mater Sci 2013;80:113 – 122.

[13] McGinty, R.D., McDowell, D.L.. J Eng Mater Tech 1999;121:203–209.

[14] Peirce, D., Asaro, R.J., Needleman, A.. Acta Metall 1983;31(12):1951 – 1976.

[15] Huang, Y.. Tech. Rep. MECH 178; Harvard University Report; 1991.

[16] McGinty, R.D., McDowell, D.L.. J Eng Mater Tech 2004;126:285–291.

[17] Evers, L.P., Parks, D.M., Brekelmans, W.A.M., Geers, M.G.D.. J Mech Phys Solids 2002;50:2403–2424.

[18] Raabe, D., Roters, F., Zhao, Z.. Mater Sci Forum 2002;396-402:31–38.

[19] Raabe, D., Zhao, Z., Park, S.J., Roters, F.. Acta Mater 2002;50(2):421 – 440.

[20] Zhao, Z., Roters, F., Mao, W., Raabe, D.. Adv Eng Mater 2001;3:984–990.

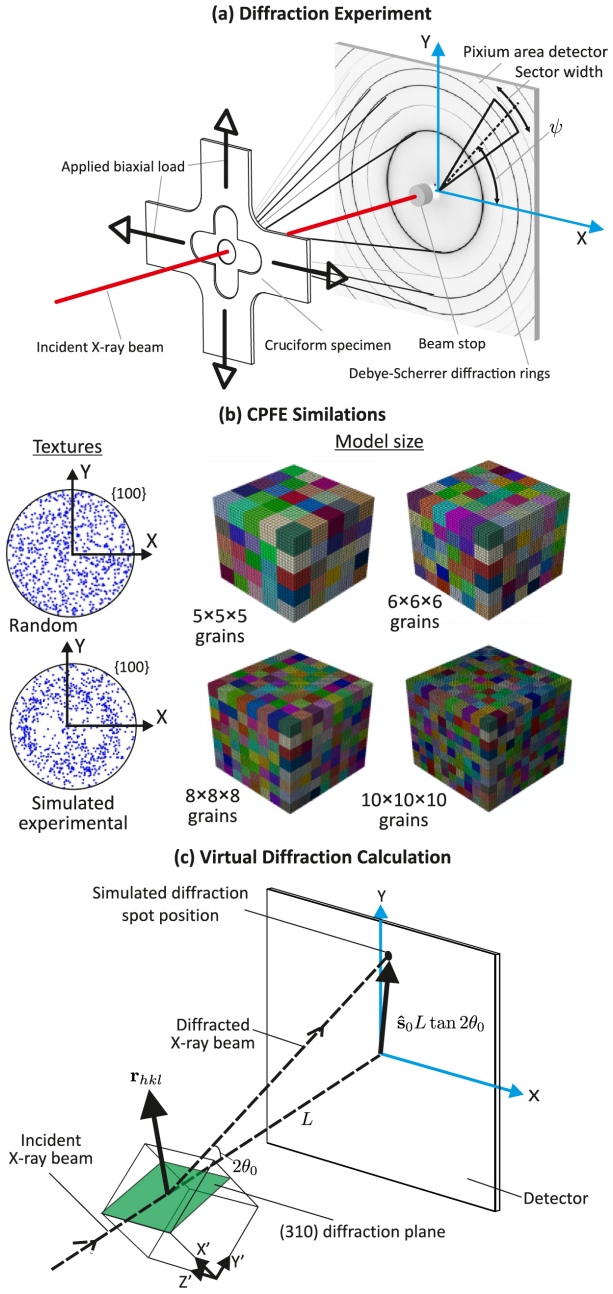

Figure 1: (a) Experimental setup at Diamond Light Source, (b) modelled CPFE polycrystals with differing numbers of grains and (c), a schematic of the computational approach to simulate diffraction from an example {310} lattice plane.

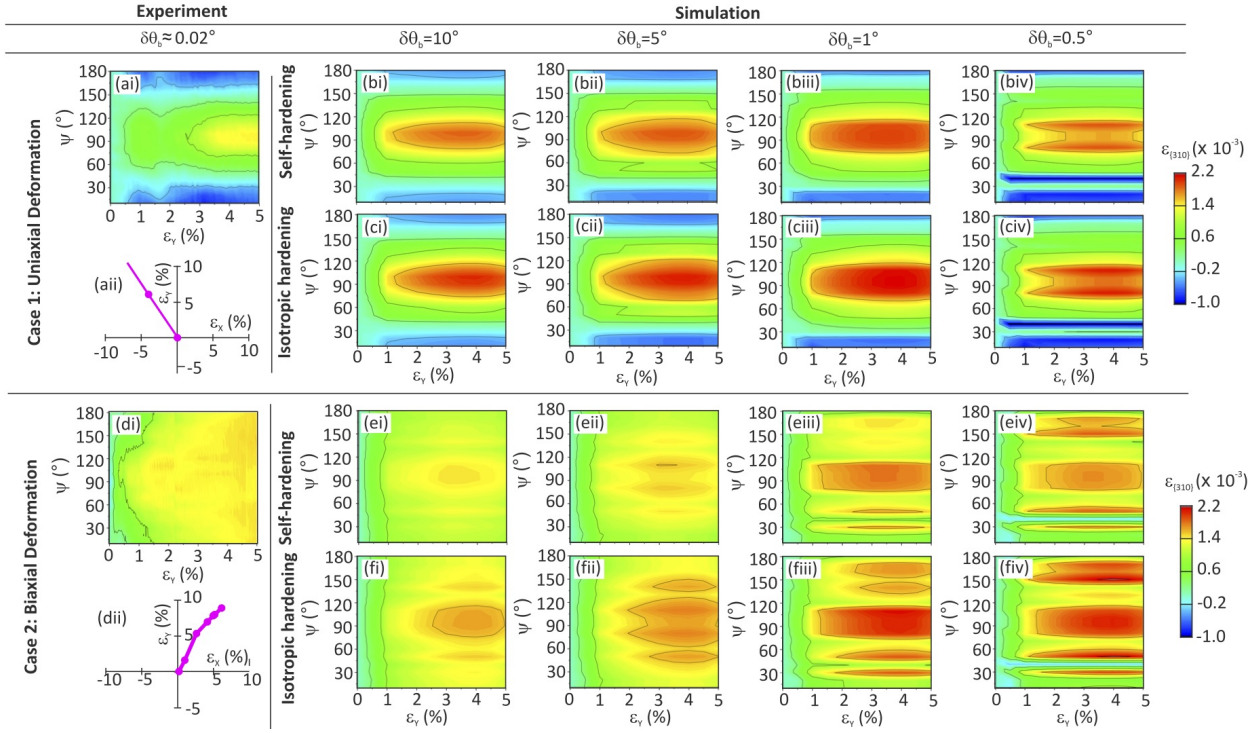

Figure 2: (a) Evolution of {310} lattice strain during uniaxial or biaxial straining from (a) & (d) experimental measurements, and (b,c) & (e,f) simulation from crystal plasticity models. Simulation results are shown with a varying tolerance of the Bragg condition, for self-hardening in (b) & (e) and isotropic hardening in (c) & (f).

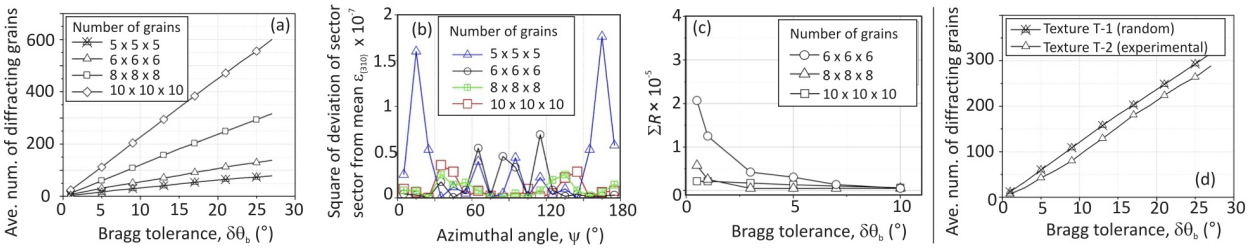

Figure 3: The effect of model size on (a) the number of diffracting grains with varying Bragg tolerance for a random texture, (b) the scatter between the mean and sector {310} lattice strains for simulated {310} lattice strains (random texture), and (c) the agreement between simulated and expected lattice strains for a simulated experimental texture with varying Bragg tolerance. The influence of texture and Bragg tolerance on the number if diffracting grains is shown in (d).

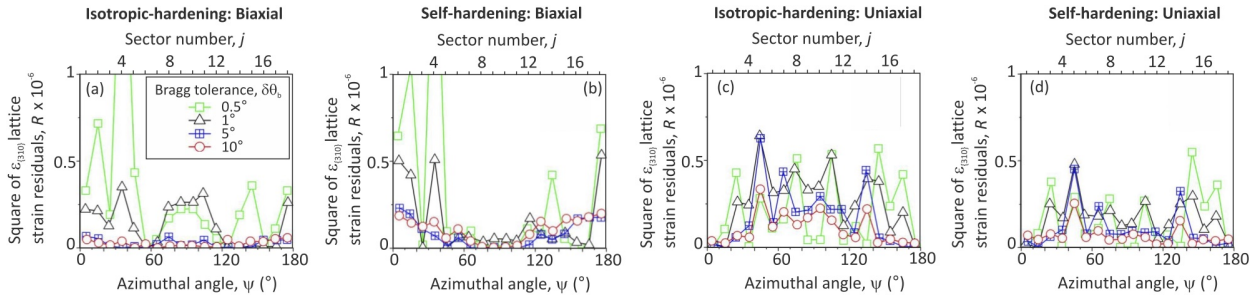

Figure 4: Comparison of residuals, R, between experimental and calculated lattice strain under (a & b) biaxial and (c & d) uniaxial deformation. Different hardening models are also compared with (a) & (c) subjected to isotropic hardening, and (b) & (d) subjected to self-hardening.

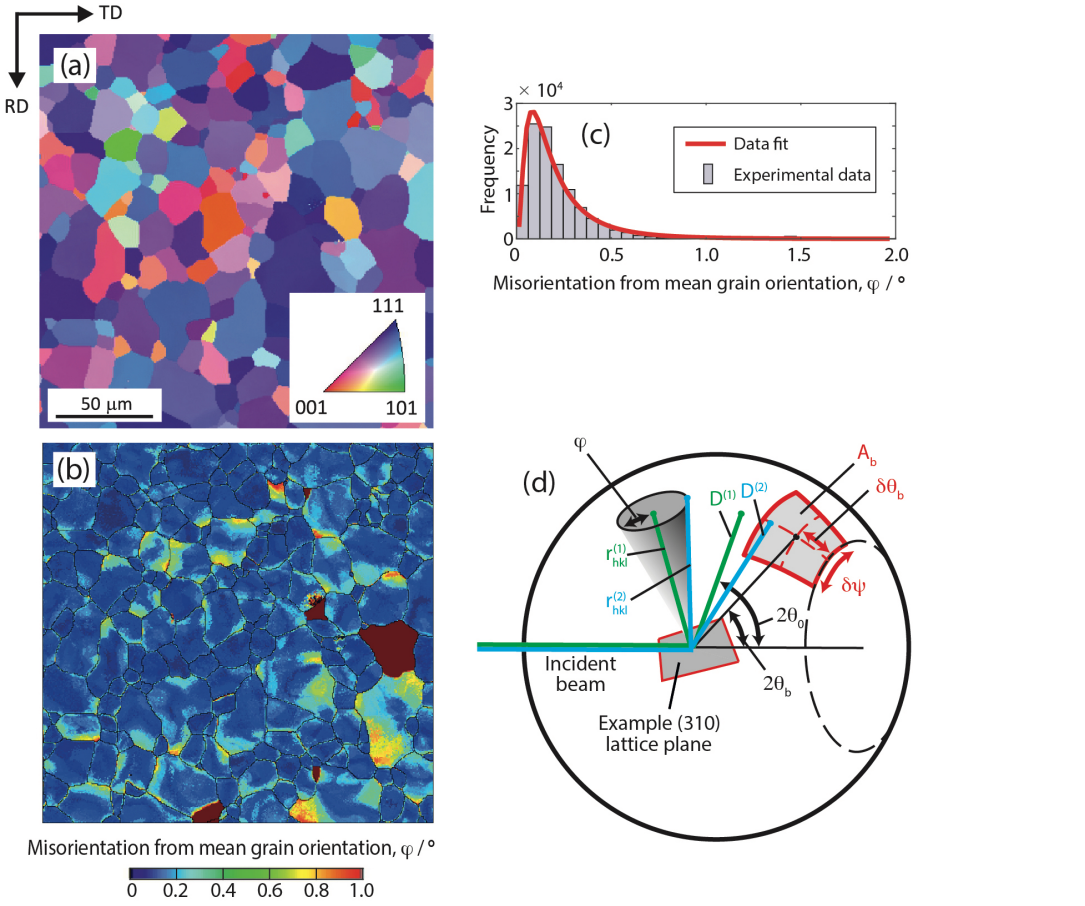

Figure 5: (a) Electron backscatter diffraction inverse pole figure map of annealed DX54 steel, adapted from [5]. The corresponding misorientation angle (calculated from the mean grain orientation) shown as a map in (b) and a histogram in (c). Geometry for calculating number of diffracting planes (d).